



Article

SAR Image Simulation of Complex Target including Multiple Scattering

Cheng-Yen Chiang ¹, Kun-Shan Chen ^{1,2,*}, Ying Yang ³, Yang Zhang ¹ and Tong Zhang ²

¹ School of Information Engineering, Xuchang University, Xuchang 461000, China; Cheng-Yen.Chiang@ieee.org (C.-Y.C.); zhangyang@xcu.edu.cn (Y.Z.)

² College of Geomatics and Geoinformation, Guilin University of Technology, Guilin 541004, China; zhangtong@glut.edu.cn

³ School of Electronic and Optical Engineering, Nanjing University of Science and Technology, Nanjing 210094, China; yangying@njust.edu.cn

* Correspondence: chenks@glut.edu.cn

Abstract: We present a GPU-based computation for simulating the synthetic aperture radar (SAR) image of the complex target. To be more realistic, we included the multiple scattering field and antenna pattern tracking in producing the SAR echo signal for both Stripmap and Spotlight modes. Of the signal chains, the computation of the backscattering field is the most computationally intensive. To resolve the issue, we implement a computation parallelization for SAR echo signal generation. By profiling, the overall processing was identified to find which is the heavy loading stage. To further accommodate the hardware structure, we made extensive modifications in the CUDA kernel function. As a result, the computation efficiency is much improved, with over 224 times the speed up. The computation complexity by comparing the CPU and GPU computations was provided. We validated the proposed simulation algorithm using canonical targets, including a perfectly electric conductor (PEC), dielectric spheres, and rotated/unrotated dihedral corner reflectors. Additionally, the targets can be a multi-layered dielectric coating or a layered medium. The latter case aimed to evaluate the polarimetric response quantitatively. Then, we simulated a complex target with various poses relative to the SAR imaging geometry. We show that the simulated images have high fidelity in geometric and radiometric specifications. The decomposition of images from individual scattering bounce offers valuable exploitation of the scattering mechanisms responsible for imaging certain target features.

Keywords: SAR image simulation; GPU-based fast computation; echo signal; antenna pattern tracking



Citation: Chiang, C.-Y.; Chen, K.-S.; Yang, Y.; Zhang, Y.; Zhang, T. SAR Image Simulation of Complex Target including Multiple Scattering. *Remote Sens.* **2021**, *13*, 4854. <https://doi.org/10.3390/rs13234854>

Academic Editor: Stefano Tebaldini

Received: 18 October 2021

Accepted: 25 November 2021

Published: 29 November 2021

Publisher's Note: MDPI stays neutral with regard to jurisdictional claims in published maps and institutional affiliations.



Copyright: © 2021 by the authors. Licensee MDPI, Basel, Switzerland. This article is an open access article distributed under the terms and conditions of the Creative Commons Attribution (CC BY) license (<https://creativecommons.org/licenses/by/4.0/>).

1. Introduction

SAR echo signal simulation offers a powerful tool for understanding image characteristics. The radar backscattering is given rise by the complex electromagnetic wave interactions with the target, be it deterministic or random [1]. It is well-known that an SAR image records the scattering process; thus, amplitude and phase are included. In [2], the SAR image was generated merely from DSM (digital surface model) data for fast SAR image simulation. For the same reason, the pre-estimated backscattering coefficient with a look-up table was adopted in the SARViz to simulate the DEM landscapes [3] and extend to integrate both the 3D target and background environment [4]. The shadowing map was approximated by rasterization considering only the point-like target [3]. For double bounce, it treated the target and background separately; their wave interactions were neglected. Because the rasterization approach was used, the influence of specular reflections on surrounding objects was not taken into account, producing an amplitude-only simulated image. It means that the phase history only records the single bounce information. The reports in [5,6] implemented the multiple bouncing using the ray-tracing technique and added the speckle incoherently. These approaches were suitable for the vitalization purpose for high-resolution scenes, such as urban areas, but the complex SAR echo was

not generated. It is noted that one of the raw data simulation objectives is to enhance the understanding of SAR scattering mechanisms within the context of electromagnetic waves interaction with complex targets.

The point-like reflectivity map with phase history by pre-calculating a look-up table from DEM of a landscape was also adopted in [7,8] for a natural scene to reduce the computation burden. Extended scene simulators, such as SARAS [9] and GRECOSAR [10] that focus on complex extended landscapes, are suitable for SAR echo generation. These data include the backscattering coefficient and phase history, ideal for a follow-up focusing on algorithm development and InSAR/DInSAR applications. The SARAS [9] was extended to natural scenes using the backscattering coefficient calculated directly from the physical model. The combination of the target and background in the echo signal model was reported in [10], but they were treated separately. The target and background and their interactions, to be more realistic, need to be included. One of the core issues in the SAR raw data simulation chain is the computation of scattered fields within synthetic aperture imaging. However, it is always a compromise between image fidelity and computation costs. For fast SAR image generation, the amplitude-only simulation assumes the known reflectivity map [11]. A real-time rendering method for the SAR amplitude image generation without involving the SAR signal model was considered in [12], such that the SAR effects narrowed down to specular, diffusion, and shadow components, all separately.

To speed up the computation, the CPU node of the coarse-grained and GPU fine-grained two-step strategy was adopted for a large area and applied to multiple GPU environments [13]. The NVIDIA OptiX sped up ray tracing, but only amplitude simulation was demonstrated for large scenes [14]. Previous studies reported a GPU implementation for different SAR acquisition geometries. The SAR echo signal was simulated by GPU using a point scatter signal model [15]. Using the point target method, the authors in [16] presented a simulator for the Spotlight mode. The authors of [17] implemented the Stripmap simulations, in which the GPU was realized for the SAR echo signal and focusing but only at a zero squint angle. Furthermore, the airborne bistatic geometry to generate the SAR echo was implemented on a dual-GPU configuration [18]. Similar to [4], we summarize the above-reviewed simulators in Table 1.

Table 1. Summary of selected SAR simulation techniques.

Data Type	Techniques	Speedup	Simulator		
Raw data	Point target model	CPU	SARSIM (Pike, 1985) [8] (Zhang, 2014) [13]		
		GPU	(Yu, 2014) [15]		
			(Wang, 2013) [16]		
			(Chen, 2011) [18]		
			(Holtzman, 1978) [7]		
		Scene area	Physical model	background	CPU
Target and background separated	CPU			GRECOSAR (Margarit, 2006) [10]	
		Reflectivity map	CPU	(Zhu, 2009) [11]	
Image	Point target model	CPU	(Sheng, 2005) [2]		
		GPU	(Sheng, 2013) [17]		
		CPU	(Mametsa, 2002) [5]		
			Scene area	Ray-tracing with rendering	(Lu, 2009) [12]
					(Liu, 2013) [14]
	Rasterization by look-up tables	CPU	SARViz (Balz, 2009) [3]		

From the above reviews, it is clear that there is a need for an efficient SAR signal and image simulator, including the SAR echo signal generation considering the coherent integration of the target and background. This simulator can also simulate incident wave rays and the propagation into the inter- and intra-interactions of targets and background clutter. The clutter and speckle are coherently given. Besides, the SAR geometry can be flexible to accommodate different SAR acquisition modes under sensor path trajectory variations. This paper aims to coherently integrate all the signal chains, starting from radar signal transmission to final image focusing, emphasizing the fast computation of the multi-frequency backscattering field in the course of synthesis aperture imaging.

In the next section, we briefly introduce the SAR signal model to facilitate the fast computation algorithm implementation in Section 3. An accumulated speedup table is summarized to validate the performance of parallel computation. Section 4 illustrates a model-based SAR simulation of the MSTAR-like 3D CAD model and multiple target's aspect angles. Finally, we provide a summary of the SAR simulation with a high parallelization performance to close the paper.

2. Basics of SAR Imaging

2.1. Signal Model

Referring to Figure 1, the SAR echo signal in the time domain results from a scattered field $E_s(\tau, \eta)$, also called the reflectivity field, convolving with the radar system impulse response, by the theory of the linear system and point spread function, $PSF_\tau(\tau, \eta)$, and is mathematically expressed as, assuming a pulse radar:

$$\begin{aligned} S_0(\tau, \eta) &= E_s(\tau, \eta) \otimes PSF_\tau(\tau, \eta) \\ &= E_s(\tau, \eta) \otimes \left[p_r\left(\tau - \frac{2R(\eta)}{c}\right) g_a(\eta - \eta_c) \cdot \exp\left\{-j4\pi f_c \frac{R(\eta)}{c}\right\} \exp\left\{j\pi a_r \left[\tau - \frac{2R(\eta)}{c}\right]^2\right\} \right] \end{aligned} \quad (1)$$

where \otimes is the convolution operator. If the SAR system resolution is ideal, perfect reconstruction of the target, or the point target model is used, then the convolution operator in Equation (1) is replaced by a multiplication operation. Where τ, η represent the fast time and slow time, respectively; R is the SAR range to the center of footprint and varies with the slow time; a_r is the chirp rate; f_c is the carrier frequency; and $p_r(\cdot)$ is the pulse waveform function of fast time [1]. R_0 is the shortest distance. The range migration along the azimuth direction from cell to cell is illustrated using a point target response. We note that in this study, the scattered field is not modeled as a collection of point targets to fully consider the single scattering and multiple scattering.

Equivalently, the echo signal in the frequency domain with linear frequency modulation in the chirp signal can be given by taking the Fourier transform of Equation (1) in fast time τ :

$$\begin{aligned} S_0(f_\tau, \eta) &= \vec{E}_{s_f}(f_\tau, \eta) \times PSF_{f_\tau}(f_\tau, \eta) \\ &= \vec{E}_{s_f}(f_\tau, \eta) \times \left[P_r(f_\tau) g_a(\eta - \eta_c) \times \exp\left\{-j \frac{4\pi(f_c + f_\tau)R(\eta)}{c}\right\} \exp\left\{-j\pi \frac{f_\tau^2}{a_r}\right\} \right] \end{aligned} \quad (2)$$

In the time domain, we need to calculate the convolution for each azimuth line with the reflectivity field within the instantaneous footprint area at a specific azimuth slow time. Based on the fast Fourier transformation, the time complexity can be significantly reduced. $P_r(\cdot)$ is the Fourier transform of $p_r(\cdot)$ and g_a denotes the azimuthal antenna pattern with a typical form [19]:

$$g_a(\eta - \eta_c) \cong \sin c^2 \left\{ \frac{0.886 \cdot \theta_{diff}(\eta - \eta_c)}{\theta_{az}} \right\} \quad (3)$$

In the above equation, θ_{diff} denotes the angle difference between the beam center and instantaneous target angle; θ_{az} is the antenna beamwidth at the azimuthal direction; and η_c stands for the azimuth crossing time at the azimuth beam center. Figure 2a shows the imaging scene; the purple circle stands for the instantaneous azimuth position. According

to Equation (3), if the instant squint angle pointing to the target is zero, the antenna gain is unity. The antenna gain will drop out of the antenna beam center following the *sinc* function shown in Figure 2b. Because this effect only occurs in the amplitude, the two-dimensional amplitude for a point target is presented in Figure 2c, where the range migration can be easily seen. Note that the antenna pattern is displayed in the grey level of amplitude, which is an order of the inverse fourth power of the slant range as specified in the radar equation.

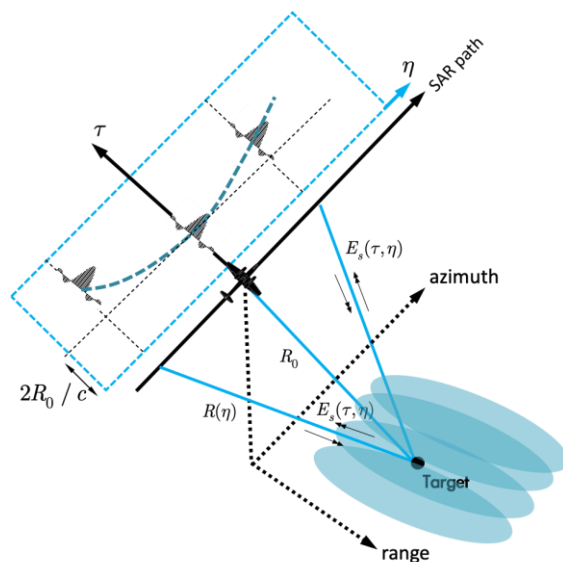


Figure 1. A side-looking SAR observation geometry; τ, η represent the fast time and slow time, respectively; $R(\eta)$ is the SAR range to the center of footprint and varies with the slow time; R_0 is the shortest distance. The range migration along the azimuth direction from cell to cell is illustrated using a point target response.

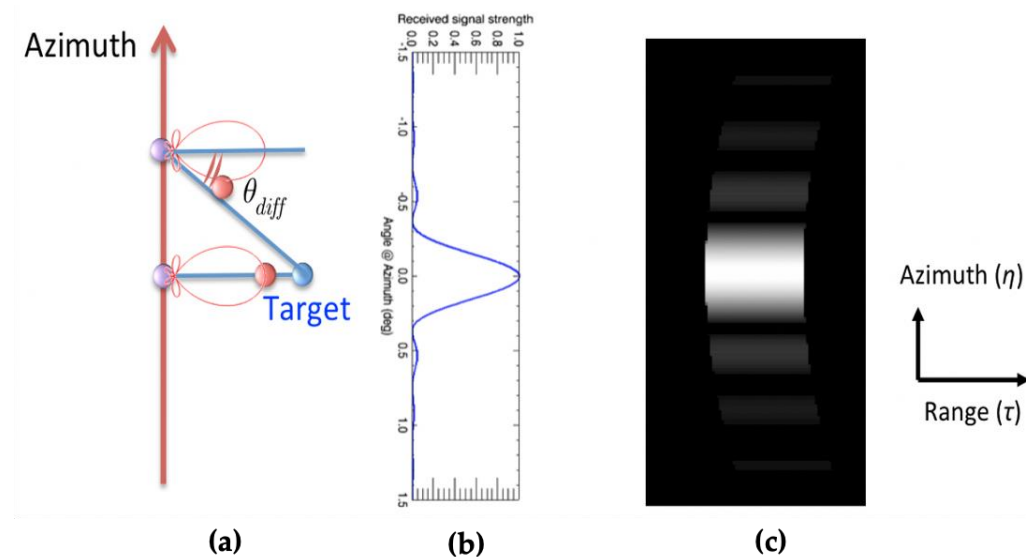


Figure 2. Azimuthal antenna pattern variations. (a) imaging scene; (b) antenna beam pattern; (c) a point target’s SAR echo amplitude.

2.2. Antenna Beam Tracking

We need to consider the antenna gain, system power loss, noise effects, and transmitted power for a more rigorous simulation. Besides, the simulated SAR image can reveal the geometry structure and preserve the radiometric and polarimetric information. To account for the antenna gain variations, we need to define the antenna angle. In Figure 3a, η_1

and η_2 denote the starting and ending positions in the course of the synthetic aperture, respectively. For an arbitrary position, let Φ_{scan} denote the azimuth angle covering the target region within the footprint, and Φ' the azimuth angle measuring from the beam center to directly to the center of the target. All signal scattering from the target region contributing to a single range bin are coherently integrated. For an acquisition mode, as shown in the figure, the azimuth scan angle is:

$$\Phi_{scan}^i = \min(\Phi_{3dB}^i, \Phi_{target}^i), i \in [\text{azimuth}, \text{range}] \quad (4)$$

where Φ_{3dB}^i and Φ_{target}^i denote the covering angle of the antenna 3dB beamwidth and target region, respectively. Note that the squint angle effect, θ_{sq} , needs to be taken into account in calculating Φ_{scan}^i . The pointing direction changes depending on the acquisition mode, e.g., Stripmap or Spotlight. Φ' is fixed in Stripmap mode but varies in Spotlight mode with the azimuth position relative to the scene center.

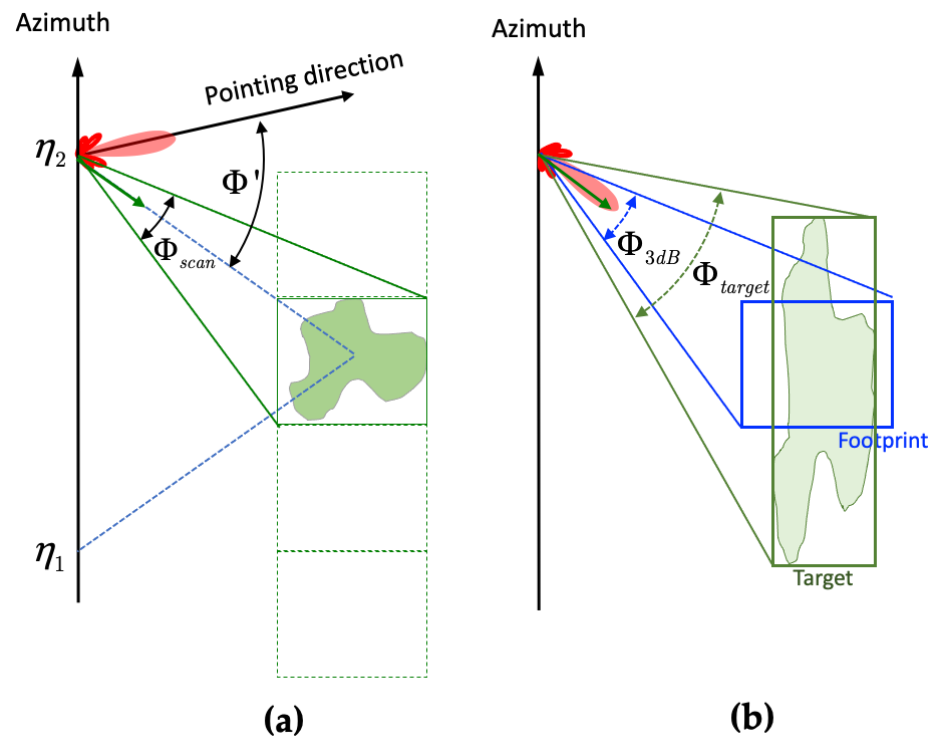


Figure 3. Azimuth antenna angle relative to a target within the footprint: (a) The antenna beam covering region with an arbitrary angle; (b) The minimum antenna beam covering for the huge target.

3. Computation of SAR Backscattering Field

3.1. An Iterative Shooting Bouncing Ray

In Shooting Bouncing Ray (SBR) [20], geometric optics (GO) is utilized to describe the electric field direction and energy propagation into and away from the target being imaged. We use the bounding volume hierarchy (BVH) method [21] to build the 3D target model. In general, the target surface is curved. Figure 4a displays a 3D CAD model of the T72 tank. When imaging by SAR, the incident and scattered waves into the target and out of it are complex; together with BVH in SBR, we can determine which triangle patch is inter-sectioned by the specific ray using a fast ray-box intersection algorithm. The intersection point on this triangle patch and the reflection vector can be calculated from Snell's law. The number of bouncings is iteratively determined according to the target's geometry complexity until preselected criteria are met. The target can be multi-layered dielectric coatings on PEC or pure dielectric, for example.

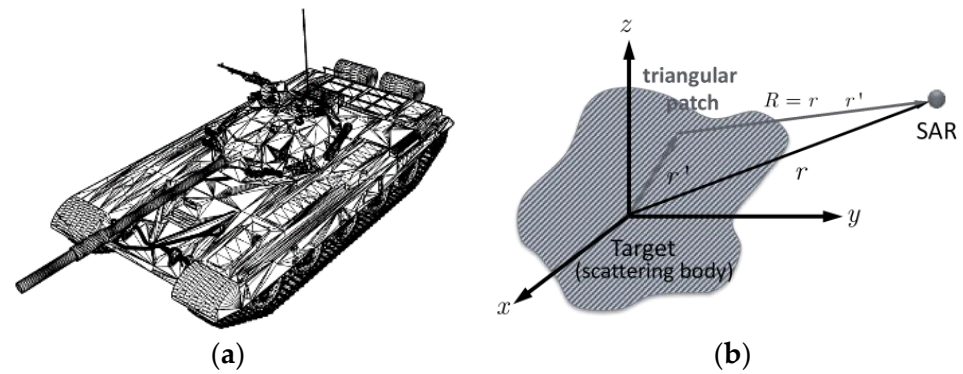


Figure 4. Geometry of scattering from a single patch on a complex target: (a) A 3D CAD model of a complex target (T72 tank in this example) (b) A single patch scattering.

By including multiple bounces, Equation (1) can be rewritten as a coherent sum of every single bounce ($m = 1, 2, \dots, \infty$):

$$S_0(f_\tau, \eta) = \sum_{m=1}^{\infty} \vec{E}_{s_f}(f_\tau, \eta; m) \times \left[P_r(f_\tau) g_a(\eta - \eta_c) \times \exp\left\{-j \frac{4\pi(f_0 + f_\tau) R_c(\eta)}{c}\right\} \exp\left\{-j\pi \frac{f_\tau^2}{a_r}\right\} \right] \quad (5)$$

$$\vec{E}_{s_f}(f_\tau, \eta; m) = \sum_{k=1}^N e_s(f_\tau, \eta; k) \exp\left\{-j \frac{4\pi(f_0 + f_\tau) R_{m,k}(\eta)}{c}\right\} \quad (6)$$

where R_c is the slant range from the target's origin to the sensor's instantaneous position; $R_{m,k}$ is the relative slant range of the target's origin and the k -th intersection point on the target for the ray-racing technique; and $|\vec{R}| = |\vec{r} - \vec{r}'|$. The field $\vec{E}_{s_f}(f_\tau, \eta; m)$ is the scattering electric field of the m -th bounce; $e_s(f_\tau, \eta; k)$ stands for the component of the scattering electric field in the k -th ray of the N , the number of the rays tracing determined by SBR [20]. In computing Equation (5), we assume the "stop-and-go" SAR signal model [19]. The amplitude of the electric field weakens with an increasing number of bouncing. In what follows, we shall detail the SBR in the context of SAR imaging using Equation (2) as a working model to generate the received signal or the SAR raw data.

In the incident surface, the spherical surface is needed to satisfy the requirement of the near and far field conditions. The smallest cell size, Δ_{LW} , on which the wave incidences and is determined by $\Delta_{LW} = 2L \tan(\theta_p)$, where L is the distance from the pseudo origin of the spherical surface to the shell of this sphere; and the Δ_{LW} relative to the smallest angle, θ_p , should be at least less than one-sixth of the radar wavelength [8]. By this, the minimal spanning angle of this incident surface grid in the vertical and horizontal directions is calculated by the eight projection points of embracing hexahedron projection on the incident surface following the ways shown in Figure 3. Based on the spanning angle and direction, the two tangential unit vectors and minimum sizes of the grid cells are determined.

3.1.1. Electric Field in Sphere Coordinate

Referring to Figure 5, at the SAR sensor coordinate, the origin of the incident electric field is (s_x, s_y, s_z) , with the instantaneous incident electric field at (x_0, y_0, z_0) , with θ_i and ϕ_i representing the radar incident angle and azimuth angles, respectively. The incident field impinges upon the target's surface (x_1, y_1, z_1) at target coordinate (x_c, y_c, z_c) with the local incident angle θ_{ic} . The target coordinate is defined by both the incident vector $\hat{i} = [x_0, y_0, z_0]$ and the target's surface normal vector $\hat{n} = -\hat{z}_c$:

$$\begin{cases} \hat{x}_c = \hat{m} \times \hat{n} \\ \hat{y}_c = -\hat{m} \\ \hat{z}_c = -\hat{n} \end{cases} \quad (7)$$

where \hat{m} is the unit vector perpendicular to the target’s surface, $\hat{m} = \hat{i} \times \hat{n}$. It follows that the local incident angle θ_{ic} can be found as:

$$\theta_{ic} = \cos^{-1}(-\hat{i} \cdot \hat{n}) \tag{8}$$

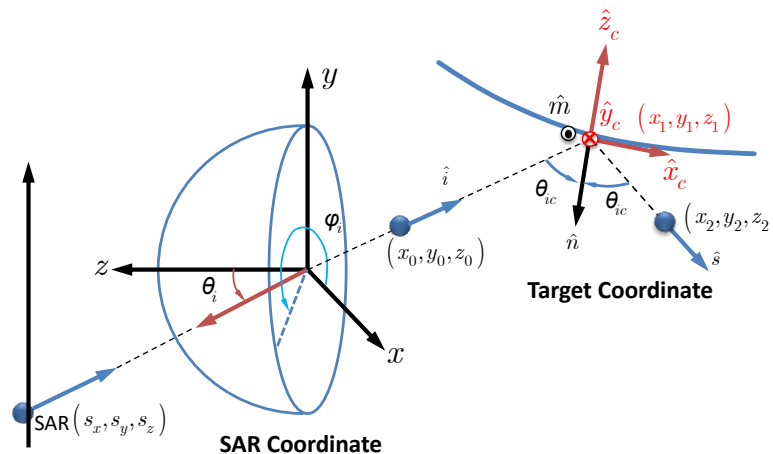


Figure 5. Geometry of SBR, modified from [20].

From the Snell’s law, the reflection direction $\hat{s} = [x_2, y_2, z_2]$ can be readily obtained.

3.1.2. Coordinate Transformation

At this point, we need to transform each patch from the local coordinate to the global coordinate. Referring to Figure 6, the transformation between the global coordinate and the local patch coordinate is by matrix [1,22]:

$$\begin{aligned} T_{global \rightarrow local} &= T' T'' \\ T_{local \rightarrow global} &= (T' T'')^{-1} \end{aligned} \tag{9}$$

where:

$$T' = \begin{bmatrix} \cos \theta & \sin \theta & 0 \\ -\sin \theta & \cos \theta & 0 \\ 0 & 0 & 1 \end{bmatrix} = R_z(-\theta) \tag{10}$$

$$T'' = \begin{bmatrix} \cos \phi & 0 & -\sin \phi \\ 0 & 1 & 0 \\ \sin \phi & 0 & \cos \phi \end{bmatrix} = R_y(-\phi) \tag{11}$$

where the azimuth and polar angles are $\theta = \tan^{-1}\left(\frac{n_y}{n_x}\right)$, $\phi = \cos^{-1}(\hat{z} \cdot \hat{n})$, with \hat{n} being the unit normal vector $[n_{x''}, n_{y''}, n_{z''}]^T = T_{global \rightarrow local} [n_x, n_y, n_z]^T$, where $n_{z''}$ is always one.

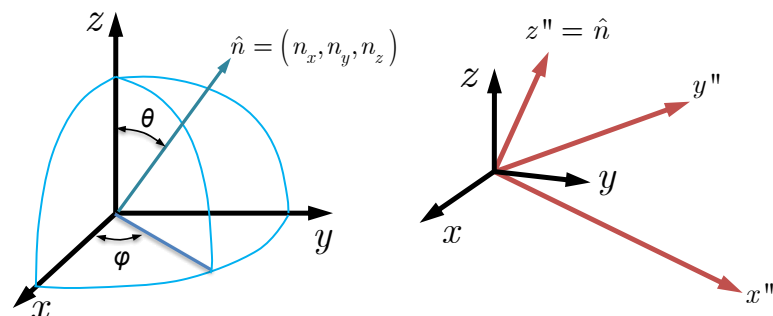


Figure 6. Global (Left) coordinate (x, y, z) and local (Right) coordinates (x'', y'', z'') [22].

3.2. Surface Current Density and Scattered Field

The far-field scattered field due to the surface current density:

$$\vec{E}_s(r, \theta, \phi) = \frac{-jk}{4\pi r} e^{-jkr} \iint_A [\eta_0 \vec{J}_s + \hat{k}_s \times \vec{M}_s] e^{jk|\vec{R}|} ds \quad (12)$$

where A is the illuminated area, η_0 is the intrinsic impedance, and $|\vec{R}|$ is the project length from \vec{r}' to \vec{r} . The surface current sources come from the electric current density \vec{J}_s and magnetic current density \vec{M}_s .

Once the surface current density is known, the scattered field can be calculated. Numerous fast computation algorithms have been proposed in the frequency domain or time domain [23]. Although the solutions may be accurate, they are still computationally prohibitive for an electrically large and complex target for SAR image simulation. As we already saw from Equation (1), the scattered field must be repeatedly calculated when SAR moves because the incident wave direction changes. If we further consider the target orientation to build a complete SAR image database, the computation of the scattered fields would stall, if not stop, the simulation.

For the target under consideration, we assume each patch has a tangent plane such that physical optics (PO) approximation can be applied to obtain the surface current density \vec{J}_s, \vec{M}_s in the illuminated region:

$$\vec{J}_s = (1 - R_v)\hat{n} \times \vec{H}_v^i + (1 - R_h)\hat{n} \times \vec{H}_h^i \quad (13)$$

$$\vec{M}_s = -(1 + R_v)\hat{n} \times \vec{E}_v^i - (1 + R_h)\hat{n} \times \vec{E}_h^i \quad (14)$$

where R_v and R_h are the Fresnel reflection coefficients for vertical and horizontal polarizations, respectively; \vec{E}_p^i and \vec{H}_p^i where $p = \{v, h\}$ are the p-polarized incident electric and magnetic fields, respectively. For a perfectly electric conducting (PEC) target, $\vec{J}_s = 2\hat{n} \times \vec{H}_h^i$ and $\vec{M}_s = 0$. For multi-layered dielectric targets, the reflection coefficients can be calculated by a recursive formula given in [24].

Under the PO approximation, the scattered is denoted by $\vec{E}_s^{\rightarrow po}$. The scattering is from the local tangent planes from every patch and the wedges in a triangular patch. We use the physical theory of diffraction (PTD) to include the diffraction field produced by the fringe current at or near edges. The diffraction currents on the dielectric edges are given by [25]:

$$\vec{I}_e = \frac{2j\hat{t} \cdot (\hat{t} \cdot \vec{E}^i)}{k\eta_0 \sin^2 \gamma} R'_v f(\delta) \quad (15)$$

$$\vec{I}_m = \frac{2\eta_0 j\hat{t} \cdot (\hat{t} \cdot \vec{H}^i)}{k \sin^2 \gamma} R'_h g(\delta) \quad (16)$$

where \hat{t} is the unit vector tangent to the edge, γ is the angle between the edge and the incident or diffracted direction, δ is the angle between the incident direction and the top surface of the wedge, R'_v and R'_h are the corrections for the reflection coefficients of the surfaces that form the wedge given in [25], and f, g are the Ufimtsev's diffraction coefficients for the Keller's cone case [26]. The diffracted field due to the diffracted currents given by Equations (15) and (16) is [26]:

$$\vec{E}_d = \nabla \times \nabla \times \frac{\eta_0}{jk} \int_C \vec{I}_e \frac{e^{jkr}}{4\pi r} d\ell + \nabla \times \int_C \vec{I}_m \frac{e^{jkr}}{4\pi r} d\ell \quad (17)$$

where r is the distance from an element on the contour C to the observation point, and $d\ell$ is the differential length along the edge discontinuity length C . The diffracted field \vec{E}_d is the correction to \vec{E}_s such that the total estimated scattered field is:

$$\vec{E}_s(r, \theta, \phi) \approx \vec{E}_s^{\rightarrow p0} + \vec{E}_d \quad (18)$$

The scattered field given in Equation (18) is in global coordinate and is transformed to local coordinate through Equation (9) before being substituted into Equation (4) for an instantaneous azimuth position. Computations continue as SAR is imaging the targets during the aperture time. It is not difficult to realize that the calculation of scattered fields is heavily burdened for various SAR acquisition modes. Furthermore, the raw signal is repeatedly generated by Equation (4) for each step of receiving the scattered field.

3.3. Computation Parallelization

In the processing flow using Equation (6), computing the scattered field for each SAR azimuth position poses the highest complexity in terms of computational parallelization. The computing time complexity is $O(mn^3)$, where m is the required number of bounces, and n^3 is the equivalent number of ray beams, frequencies, and aspect angles; in common practice, n^3 is easily at least on the order of 10^9 . Our goal is to reduce the overall time complexity to $O((m + \log_2 n)n^2) \approx O(n^2 \log_2 n)$, if proper optimization is attempted and implemented. The most massive loading stems are from the inner loop of calculating the scattering electric field by integrating the surface current, governed by the integral equations, for each incident ray impinging upon the target. Inside the integration, the coordinate transformations between global and local coordinate systems are involved. Hence, to this end, the parallelization scheme based on NVIDIA CUDA includes several components described below.

We carried out the computation of scattered fields in the frequency domain for range compression. The outer loop is the essential ray-tracing element for each grid on the different incident surface mesh. The initialization of shooting and bouncing variables is declared here. The multi-frequency is involved in the next loop because the transmitted signal and scattered signal are frequency dependent with the fast ray-polygon intersection algorithm, which has the time complexity of $O(\log_2 n)$. The inner loop treading the bouncing process can be divided into five steps.

1. SBRs: We conduct the ray tracing in the outer loop and extract the information of the intersection point and the reflection direction.
2. Pre-calculation: We calculate and store the distance between the current and previous bouncing points, local coordinate transformation angle on the intersection polygon, and global coordinate transformation matrix in the cache of GPU.
3. Dielectric grid: We compute the reflection coefficients for the dielectric target for each grid on the incident ray's target.
4. Post-calculation: We conduct the ray beam area normalization and wave propagation distance in this step. The parallel and perpendicular electric field components must be projected onto the receiving plane using the relationship of the geometry matrix of the scattering field and the receiving plane in the pre-calculation given in step 2.
5. Summation: We sum up the scattered fields for all frequency components at a certain SAR look angle and the target's aspect angle, using the CUDA parallel reduction algorithm.

As illustrated in Table 2, in terms of the computation complexity for general SAR acquisition, the aspect angles are 10 to the power of 3. The ray-tracing elements are on the order of 10 to the 10 to the 7 power, the frequency steps can be 10 to the 10 to the 2–3 power, and the iteration number of multi-bouncing is between 1–10. This ends up with the overall time complexity $\sim O(n^2 \log_2 n)$. Comparatively, the number of bounces, m , is small compared to n represented by K , M , and N .

Table 2. Computation algorithm of the scattering field.

```

foreach  $K \in \text{Aspect orientation angles}$  do
   $E_{s,total} \leftarrow (0,0)$  /* Initialization */
  foreach  $M \in \text{Ray}$  do
    while  $m \neq \text{Converge Condition}$  do /* Max. bouncing detection */
       $isHit \leftarrow \text{ObjectIntersection}()$  /* Intersection procedure for all polygon */
      if  $isHit = \text{true}$  then
        foreach  $N \in \text{wavelength}$  do
           $E_s(N, M) \leftarrow \text{PO\_Diffraction}()$ 
           $E_{s,total} += E_s(N, M)$  /* Coherent summation to one */
        end
      end
    end
  end
end

```

Table 3 gives the computation environment, and Table 4 summarizes the cumulative speed up compared to the sequential coding (no paralleling implementation). The breakdowns clearly show the time distributions of each stage of operation. The overall speedup factor is up to 224×. This speedup, however, does not imply a limit. Using higher specifications of GPU and enhancing parallel optimization would be able to push up the speedup.

Table 3. Computing environment.

GPU Specification	
Device	Titan-X
Global Memory Size	6143 MBytes
Shared Memory Size/Block	16384 bytes
Number of Register/Block	49152
Maximum no. Threads/Block	1024
Number of Threads in Block	(1024,1024,1024)
Number of Blocks in Grid	(2147483647,65535,1)
GPU Clock Rate	0.88 GHz
CPU Specification	
Device	Intel® Core™ i7-3930K 3.2 GHz
Total Memory Size	32 GBytes
Operation System	CentOS 6.5

Table 4. Summary of the cumulative speedup.

Item	Elapsed Time [s]	Step Speedup	Cumulative Speedup
Sequential code (baseline)	560.0	1×	1×
0 Branch reduction and Memory Coalescing	6.93	80.8×	80.8×
1 Constant Variables	5.80	1.19×	96.6×
2 Split a large kernel to small kernels	4.50	1.29×	124.4×
3 Move freq. independent sections to outside of loop (Freq. and bounce loop exchange)	4.26	1.06×	131.5×
4 Reduce device memory using patch	3.84	1.11×	145.8×
5 Move partial variables to shared memory	3.23	1.19×	173.4×
6 Heavy kernel rearrange and loop unrolling	3.09	1.05×	181.2×
7 Overall use system optimization flag	2.50	1.24×	224.0×

4. Validations

We used canonical targets of the sphere and the dihedral reflectors to validate the simulation. The sensor parameters and the associated imaging parameters are listed in Table 5. The radar frequency was set to 9.6 GHz with 591 MHz of bandwidth, and four polarizations of HH, VH, HV, and VV were simulated. The path trajectory length means the SAR moving distance with a look angle of 72.64°. Using this setup, the range of the azimuthal scanning angles was relatively small, about 3.9°. For SAR data takes, we computed the backscattering field at a small step of 0.003362. We adopted the “stop-and-go” model in the simulation, so the phase ambiguity problem mainly occurs in the azimuth direction, especially in the Doppler centroid estimation. For a zero-squint, the phase ambiguity is not an issue. For a squint angle of 30 degrees, the ambiguity number is larger than one PRF. Nevertheless, we were able to obtain a reasonable estimate of the Doppler centroid frequency. We implemented a Range-Doppler algorithm (RDA) for Stripmap mode and an Omega-K algorithm (WKA) for Stoplight mode for image focusing [19]. The multi-looking cross-correlation algorithm (MLCC) and the multi-looking beat frequency algorithm (MLBF) were used to estimate the phase ambiguity.

Table 5. Summary of cumulative speedup.

Parameter	Value
Look angle	72.64°
Squint angle	0°
Sensor velocity	54.12 m/s
Sensor height	134.75 m
Path trajectory length	278.96 m
Scanning azimuth angle	−1.8501°~1.8468°, Interval = 0.0033°
Polarization	Single/Dual/Quad polarization
Center frequency	9.6 GHz
Chirp bandwidth	591 MHz
PRF	213.4 Hz
Exposure time	4.69 s
Doppler bandwidth	194.63 Hz
Resolution	Slant range: 0.2536 m, Azimuth 0.2780 m

The computations of the backscattered field during aperture synthesis are required to apply Equation (6) to obtain the SAR signal, a complex signal. Computationally, every single ray bouncing can be recorded and processed into the SAR signal. In dealing with the iterative computation of ray bouncing in Equation (6), we continued the ray tracing until the multiple scattered field amplitudes:

$$\sum_{\eta} \sum_{f_{\tau}} \left(\left| \vec{E}_{s_f}(f_{\tau}, \eta; m) - \vec{E}_{s_f}(f_{\tau}, \eta; m-1) \right| / \left| \vec{E}_{s_f}(f_{\tau}, \eta; m) \right| \right) \leq 10^{-4} \quad (19)$$

where m is m th ray bouncing as indicated in Equation (6). The convergent rate depends on the geometry complexity and dielectrics of the target. In such a way, we can better explore the scattering process and its dependence on radar and target parameters, both dielectric and geometric.

We begin simulating the sphere target; the scene consists of three spheres: a PEC and two dielectrics coated on PEC spheres. The coatings had a thickness of 0.005 m ABS1, PEC, and ABS2 coating, placed along the azimuth direction spaced uniformly 10 m apart, as indicated in Figure 7a. The diameters and dielectrics of the three spheres are given in Figure 7b. For a further inspection, we illustrate the amplitude responses of the azimuthal and range profiles for three targets in Figure 8b,c, respectively, which are all cut through the focused images' peak values in Figure 8a. Rich information can be revealed due to electromagnetic wave behavior, such as scattering and penetration, occurring concurrently. In the ABS2 target with the lower dielectric constant, much of the power penetrates through

the media. Thus, the first response is weaker than the PEC target, whereas the boundary reflection occurs with a small response. With an increase in the dielectric constant, the first response of the ABS1 becomes stronger, and the penetration energy decreases.

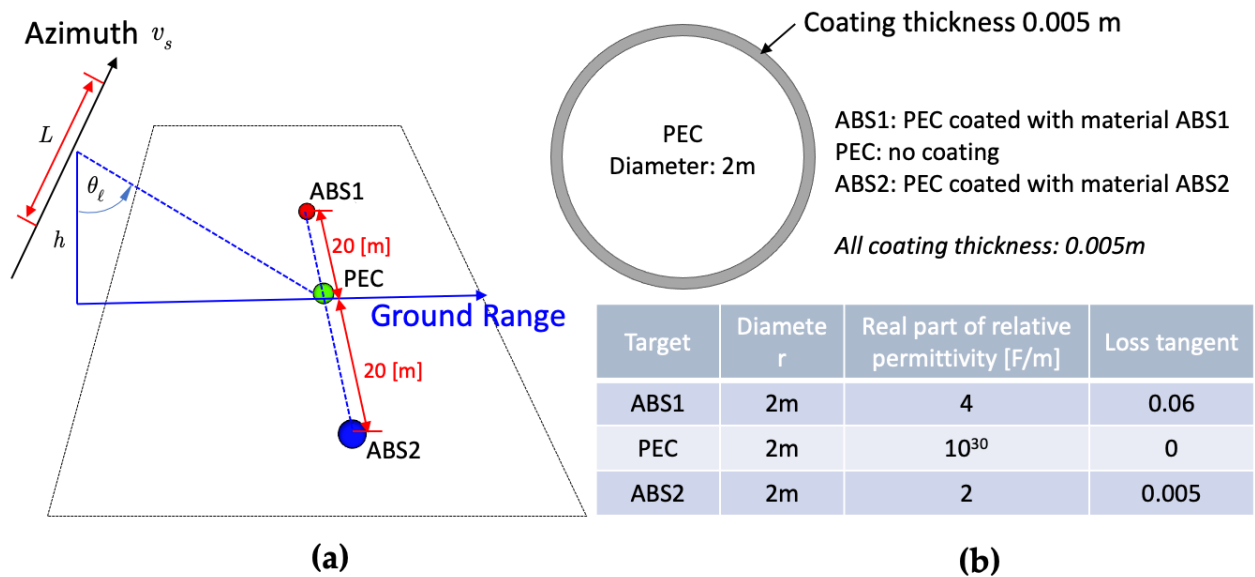


Figure 7. (a,b).Imaging scene of three spheres: PEC, PEC coating with ABS1, and ABS2, displaced along the azimuth direction. The diameters and dielectrics are shown in the table.

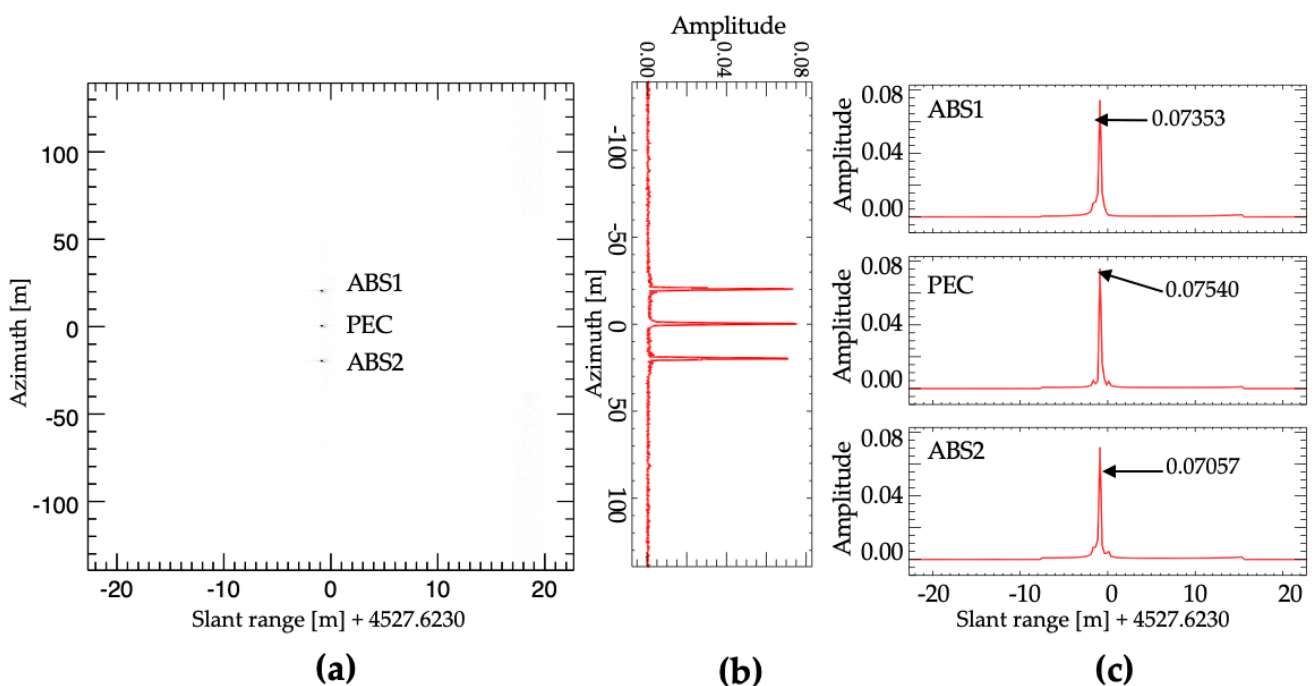


Figure 8. (a) Focused images of PEC, ABS1-coated PEC, ABS2-coated PEC spheres; (b) amplitude responses of azimuthal profiles for three targets; (c) amplitude responses of slant range profiles for three targets; the amplitude profiles are all cut through the peak values of the focused images in (a).

The canonical targets of the sphere and the dihedral reflectors, with their known scattering matrices, provide ideal targets of polarimetric calibration and polarimetric image focusing, both qualitatively and quantitatively. Figure 9 illustrates the image scene, similar to Figure 7a. Figure 9b shows HH and VH polarized RCS and the dihedral reflector RCS variation with the illumination angle, for the azimuth angles of interest. The focused

HH and VH polarized images are illustrated in Figure 9d,e, respectively. Three dihedral reflectors are identified in the HH polarized image, whereas the VH polarized image itself can appear due to the angle dependency and edge effect of the dihedral reflectors. The HH polarized image is approximately 22 dB stronger than the VH polarized image in Figure 9b. The dominant scattering of a dihedral reflector is double-bounce scattering in the HH image. In a deeper inspection of the VH polarized image, the two dihedral reflectors placed at 10 m apart exhibited their shapes in two parts. This corresponds to the VH polarized RCS return in the azimuth-frequency domain, where the VH polarized RCS is more dependent on the azimuth angle. The VH polarized RCS will be enhanced when the sensor scans away from the dihedral reflectors due to the absence of the azimuthal reflection symmetry.

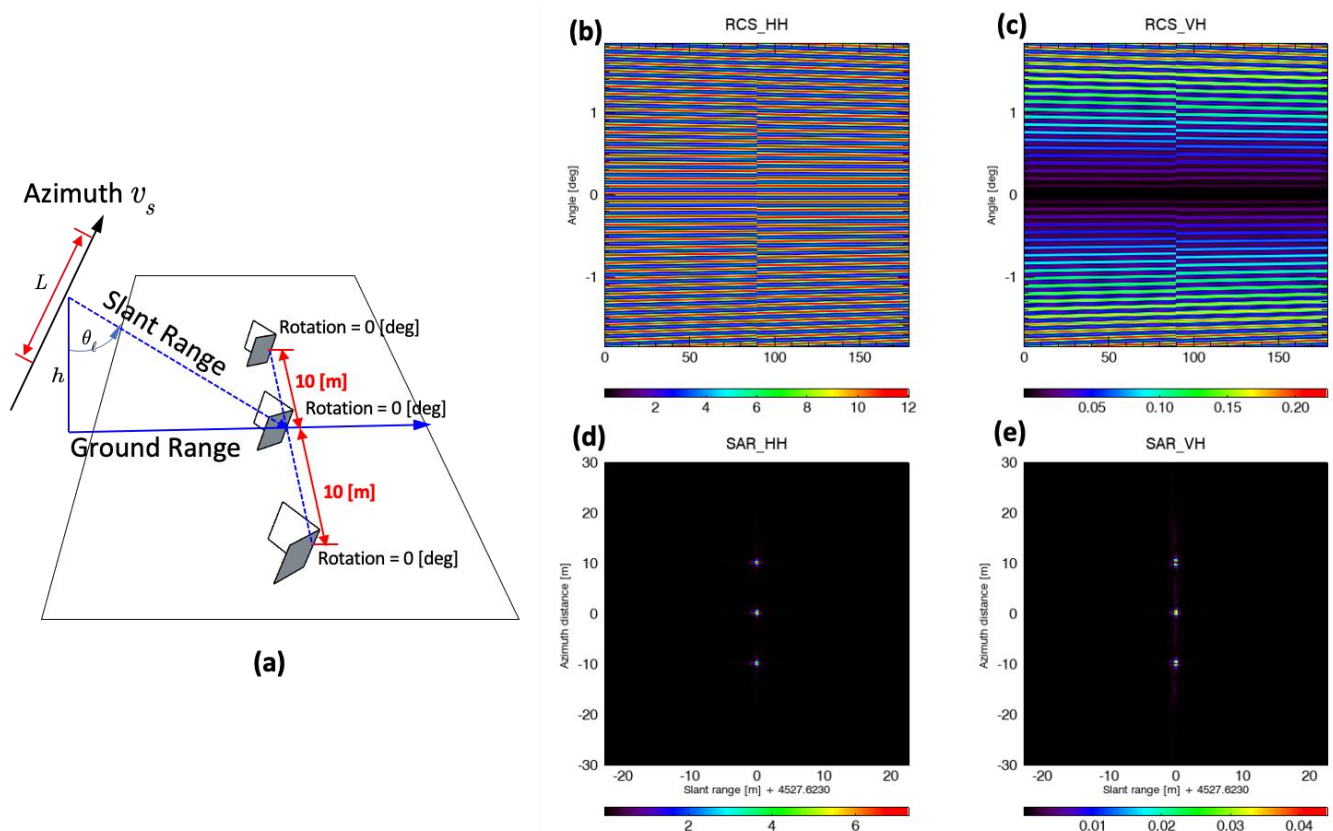


Figure 9. (a) Imaging scene of three dihedral reflectors with 0° rotation; (b,c) raw signal for HH and VH polarizations; (d,e) focused HH and VH polarized images.

In the third simulation case, the three dihedral reflectors have different orientations by rotating 0° , 22.5° , and 45° , placed along the azimuth direction with the spacing of 10 m. Figure 10a illustrates the imaging scene, while Figure 10b–e display the fully polarized focused images with HH, VH, HV, and VV respectively. We may identify the 0° -rotated dihedral reflector in the HH and VV polarized images, as is the 45° -rotated dihedral reflector in the HV and VH polarized images. We can also observe the 22.5° -rotated dihedral reflector in the fully polarized images, which agree with the theoretical scattering matrices [27].

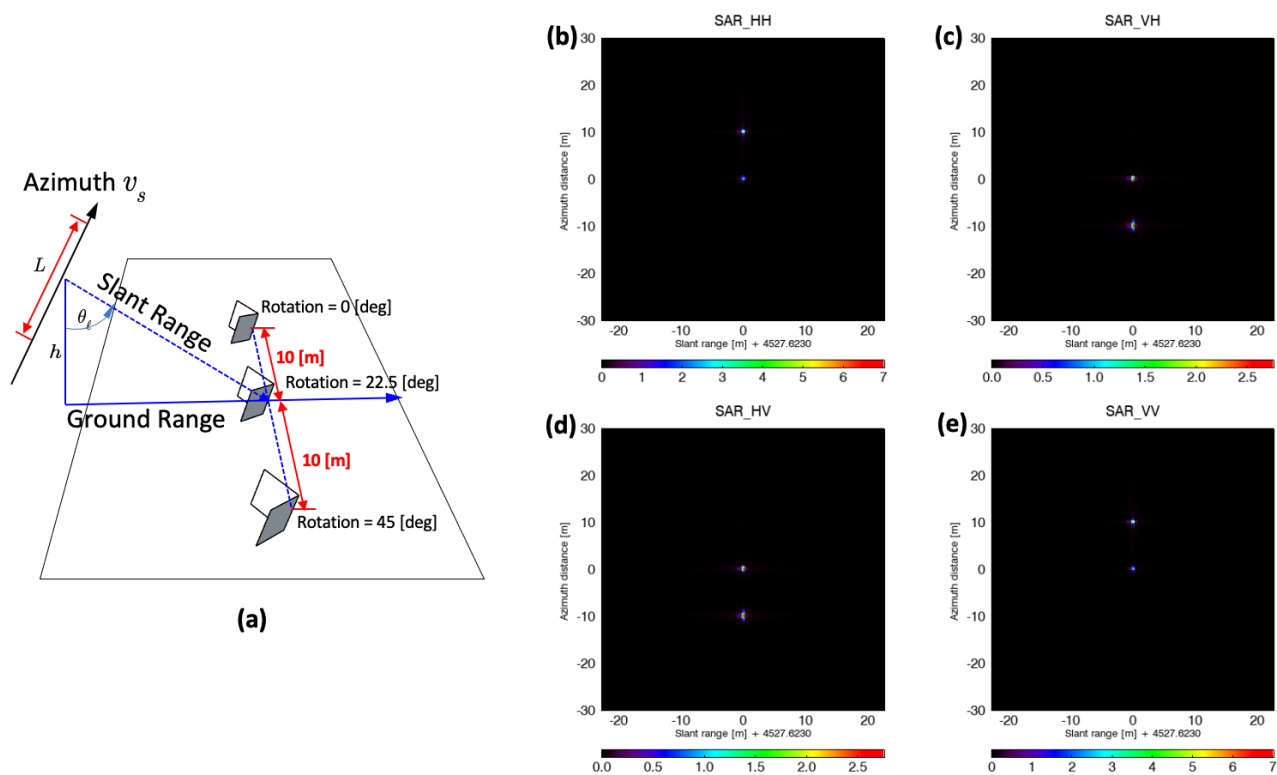


Figure 10. (a) Imaging scene of three dihedral reflectors with three dihedral reflectors with 0° , 22.5° , and 45° of rotation; (b–e) HH, HV, VH, and VV polarized focused images.

5. Examples of Simulation Images of a Complex Target

The complex targets with high structural and interaction between the target and background were presented in a section later without loss of reliability. The MSTAR dataset is a highly representative example that corresponds to our purpose flow chain to simulate a dataset. We applied this simulator to the MSTAR T72 target. The real SAR image had 1 feet resolution by the Spotlight SAR acquisition mode in the airborne system, operating at X band with high depression angle 15° and 17° .

5.1. Target CAD and Observation Setup

The target's type in the public dataset has more than 10 kinds, and there are up to almost 300 different aspect angles for each target. Because of the high acquisition look angle, we could find the shadow effect easily in the images dataset. The 3D CAD model was Autodesk 3DS Max file format with 1,086,030 polygons that triangulates from the original model [28]. The model is placed on the plane ground to examine the multi-bounce effect due to the ground surface. The aspect angles were within $[-1.8502, 1.8468]$, with an interval of 0.0033 degrees to match the PRF of 213.4 Hz, ending with 1100 samples. We adopted the sensor path trajectory with a general XYZ coordinate at an equal sensor height, and all light-of-sight was projected onto the geodetic coordinate with WGS84 datum. Because the target includes the background in the square 20 m area, we restricted the maximum observation swath to 95.6 m, resulting in 360 samples, such that the spacing was 0.2536 m.

Figure 11 shows the surrounding box with a 20 m square and 5 m height for covering the background and target. Figure 11a shows the SAR sensor using Spotlight acquisition mode directs to the target with a depression angle. A pseudo ground plane was added to the model for the double-bounding effects between the ground and the wheels. To implement the SBR, we applied an embracing bounding box for a fast ray-triangle intersection, as shown in Figure 11b. The SAR image features are sensitive to the relative orientation; different aspect angles are included in the simulation dataset. The aspect angle is defined

as the line of sight pointing to the right (see Figure 12). The aspect angle is rotated along the z-axis with the left-hand rule that is the same as the MSTAR dataset.

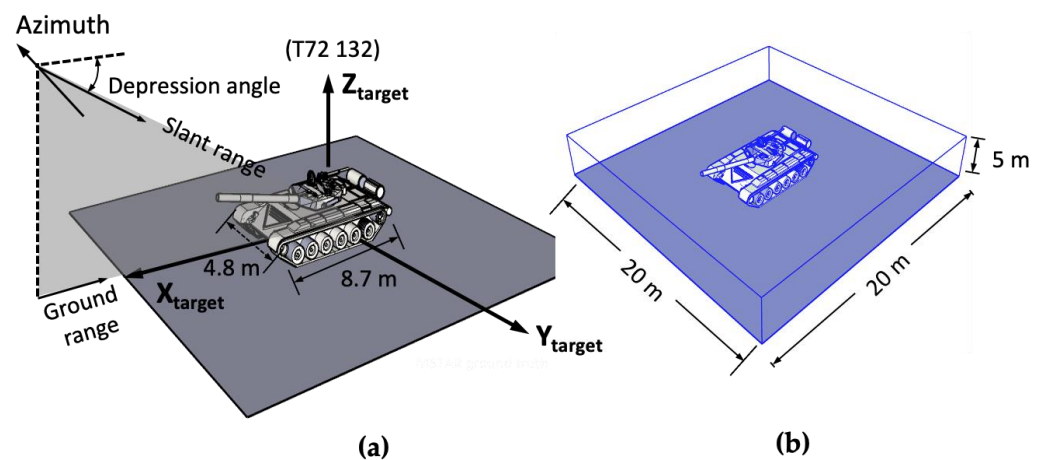


Figure 11. (a) SAR observation geometry; (b): CAD bounding box.

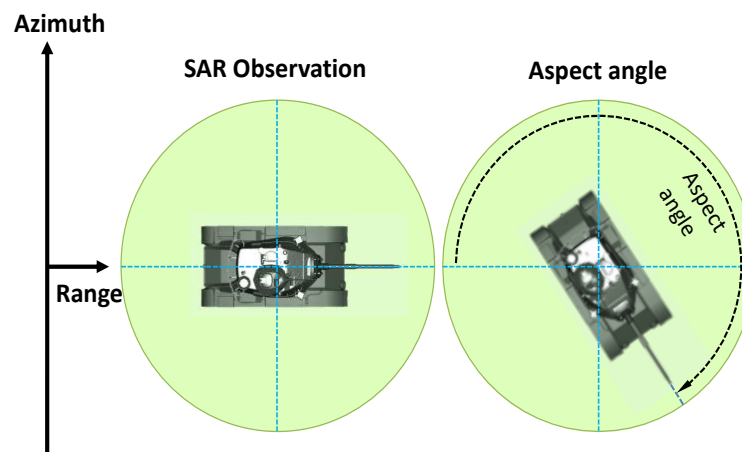


Figure 12. Definition of the target's aspect angle.

5.2. Simulation Parameters

Table 6 summarizes the simulation parameters. To be consistent with the MSTAR specifications, we used the X-band with a 9.6 GHz center frequency, 591 MHz bandwidth, and HH polarization. We calculated the antenna beamwidth, range resolution, and spacing from the effective antenna length. Note that the state vector's position and tangential velocity can be derived from the azimuth dimension and PRF. The Doppler parameters in Table 7, including the Doppler bandwidth and rate, were calculated using the antenna beamwidth and PRF. The spacing at both directions was set to almost 0.25 m to meet the 1 feet resolution requirement in real MSTAR data [29]. The scan angle range was calculated by Equation (3). The image size was 360 samples of frequency sampling in the range direction and 1100 samples of azimuth sampling for fully azimuth synthesis.

5.3. Simulated Images and Discussions

Figure 13 compares real and simulated images at 230°, 270°, and 180° aspect angles. The left column is the MSTAR actual image in amplitude. The simulated SAR amplitude images are in the middle, corresponding to the relative target's geometry, including the target's attitude and the slant and ground plane's dimension. We note that the barrel pointing direction was different: the barrel direction aligned with the vehicle body in the simulated image but was slightly offset, appearing in the real image with an unknown

angle. For example, in the 230° aspect angle, the maximum dimension at azimuth is 9.77 m or about 38 pixels. The slant range is 8.85 m, corresponding to about 35 pixels, and at the ground, the range is 9.27 m, nearly 36 pixels. From these high-resolution simulated images, we found the structure of the turret in the 230° clip. The double bouncing effect with strong scatter mainly occurs. In the 270° , the strong single and double bouncing induced by the wheels and track was shown along the azimuth direction. The barrel structure is also present here because the pointing is perpendicular to the line of sight. The two secondary fuel tank structures can also be found in the 180° clip because they are the first intersection targets with the radar incident wave.

Table 6. SAR parameters for simulating the T72 target.

Category	Parameter	Value
Radar System	Center frequency	9.6 GHz
	Chirp bandwidth	591 MHz
	PRF	213.4 Hz
	Duty Cycle	6.8 %
	Antenna size (Azimuth \times Elevation)	0.8×15 m
	Antenna effective coefficient	0.7
	Look angle	72.6367°
	Swath	95.6 m
	Distance from center of target	500 m
	Reference ellipsoid	WGS84
Image size	Range direction	360 samples
	Azimuth direction	1100 samples

Table 7. Derived variables for simulating the T72 target.

Category	Parameter	Value
Doppler coefficient	Azimuth effective antenna	0.556 m
	Doppler rate	41.4350 Hz/s
	Exposure Time	4.6972 s
	Doppler bandwidth	194.6303 Hz
Resolution & Spacing	Range resolution	0.2536 m
	Azimuth resolution	0.2780 m
	Range spacing	0.2536 m
	Azimuth spacing	0.2536 m

At this point, it is worth noting that the main factor most likely to produce the high levels of sidelobe, as shown in the simulated images of Figures 9 and 13, is due to the antenna 3 dB wide range. To speed up the echo signal generation, we limited the exposure range of the antenna, as indicated in Figure 3, to alleviate the computation burden. This exposure time gives rise to a *sinc* squared-like function to reduce the edge effect, but considerable sidelobes still appeared after image focusing. In our SAR imaging simulation, we applied a Kaiser window in the azimuth direction. We may suppress the sidelobe level in our future work by (1) expanding the physical range of the antenna gain pattern in the echo signal generation process, (2) enhancing the azimuth window filtering in the SAR imaging process, and (3) increasing the azimuth window filtering in the SAR imaging process. Methods, such as spatially variant apodization and sparsity constraint regularization, may be applied. We will attempt to implement them in our future simulations.

Figure 14 shows the GPU computation time corresponding to every aspect angle, where the calculation time is dependent on the target's pose to SAR observation. We can note a symmetry of about 180° of the aspect angle. A longer computation time was required to reach convergence in accounting for the multiple bounces in ray tracing, implying in some sense that richer image features about the target may be acquired. Table 8 shows the two extremes, the longest and shortest computation times at the 60° and 180° aspect angles.

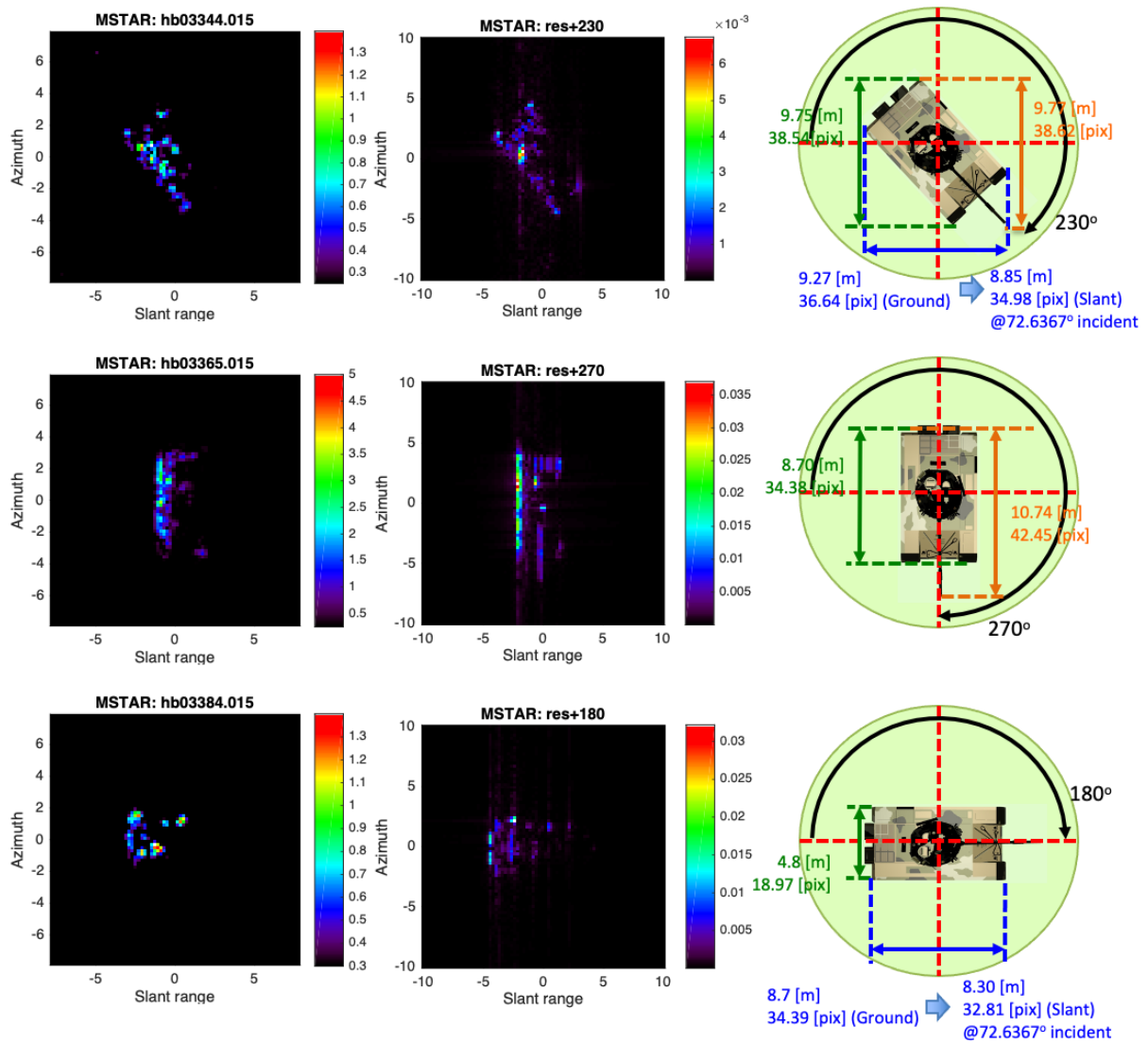


Figure 13. Comparison of real (left panel) and simulated (middle panel) images at 230° (top row), 270° (middle row), and 180° (bottom row) aspect angles defined in the right panel.

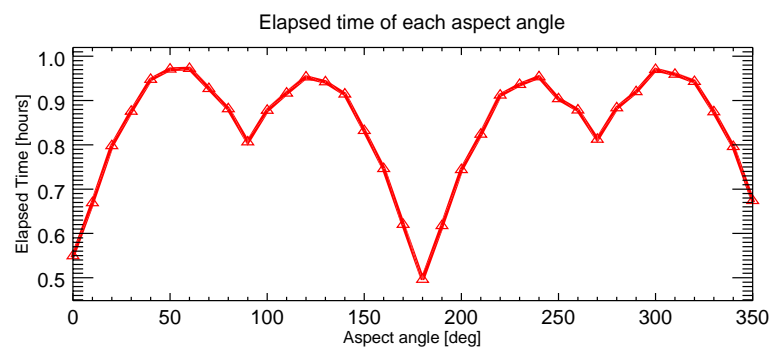


Figure 14. GPU elapsed time for each aspect angle.

Table 8. Summary of the cumulative speedup.

Aspect Angle	CPU Time	GPU Time	Speedup Rate
60°	74.70 h	0.97 h	77.0×
180°	43.46 h	0.49 h	88.7×

The image size is 360 samples of frequency sampling and 1100 samples of azimuth sampling; it took 43 and 74 h of CPU computation time. The GPU-based algorithm proposed in this paper reduces the computation time to less than an hour, with a speedup rate of more than 70 times. Compared to the $224\times$ speedup shown in Table 4, we note that for a much more complex target than in this example, the rays in SBR may go through quite different bouncing numbers. So, there will be many threads waiting for the one that takes care of the highest number of bouncing when executed simultaneously on the GPU thread. Nonetheless, the proposed GPU-based parallel algorithm offers an effective and efficient approach to simulating the SAR image of both complex geometry and electrically large targets, such as the T72 tank demonstrated in this example. This allows us to build up more complete simulated SAR images for target poses for classification and identification.

As mentioned previously, the total bouncing from the incidence to the scattering out of the target can be decomposed into individual bouncing. The scattering signal from this individual bouncing can be processed into SAR images so that the detailed interaction of the scattering process can be extracted to explore the target features. Figure 15 shows the total bouncing image after a coherent sum of the individual bouncing signal at a 220° aspect angle. To better visually inspect the image feature, we also overlaid the target's wireframe on the Figure 15a image, as shown in Figure 15b. Figure 15c–f display the simulated images from bouncing 1 to bouncing 4, denoted as level 1 to level 4. Because the signal level decreases with the increasing number of bouncing, for comparison, we normalized the image amplitude to a maximum value of 0.2. At levels higher than four bouncings, the signal is too weak and is not shown.

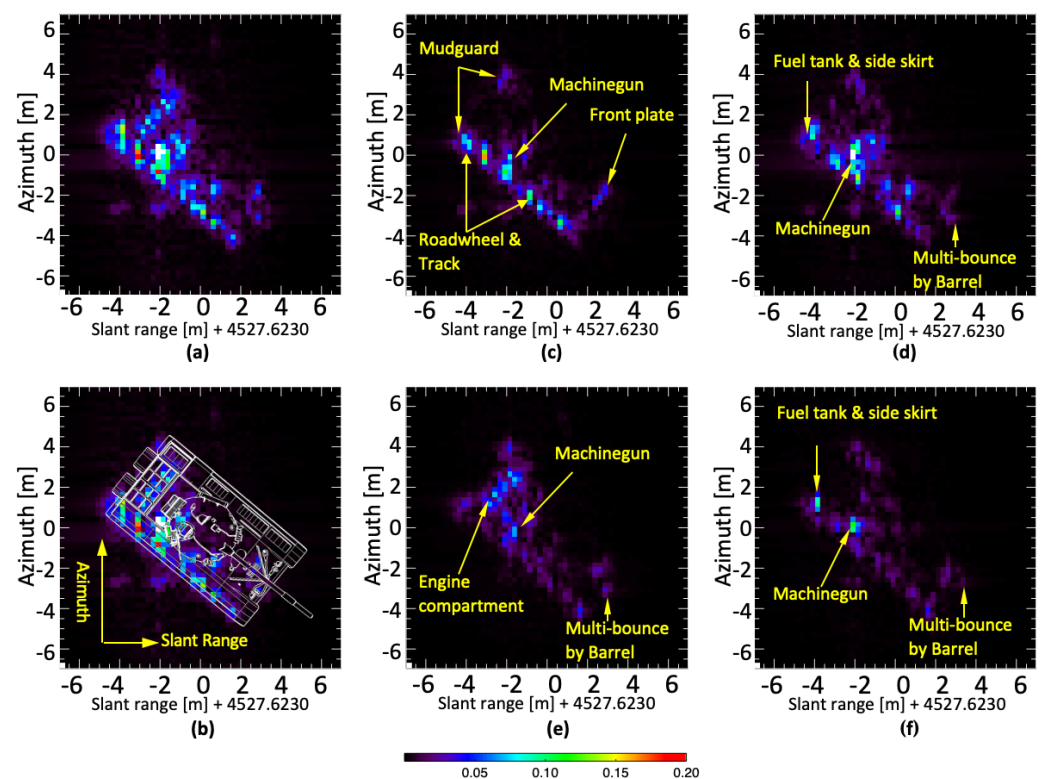


Figure 15. Target structures corresponding to the simulated SAR image features. (a) Total bouncing image, (b) overlay with the target's wireframe onto the image (a); (c) Level 1 image; (d) Level 2 image; (e) level 3 image; (f) Level 4 image. At levels higher than 4 bouncing, the signal is too weak and is not shown.

A further look reveals that the strong scattering points between the roadwheel and trace appear in level 1 and level 2 images. The structure between the roadwheel and trace is involved but is also significant for enhancement of the wave scattering. A strong scattering

phenomenon also appears in level 3 and level 4 images but with much weaker intensity. The machinegun position feature is visible in level 1 through to level 4 images and is most apparent at level 2. Because, at this pose, the machinegun placement is parallel to azimuth and is located on the turret side, it is a scattering preference. In the level 2 image, there is significant scattering at the junction of the secondary fuel tank and side skirt, considered a Dihedral-like reflection, and this is not presented in other level images. The engine compartment that appears in the level 3 image has a regular pattern across the slant range. The cooling plate produced regular patterns, which is mainly due to the contribution from level 3 after decomposition. The mudguard and side skirt features, which make up one of the most distinctive features of this target, appear at the close range but disappear as the turret is obscured at a far range due to the shadowing effect. There is a distinct feature point at the barrel and front plate junction, which gradually moves toward the far range from level 2 to level 4 due to multiple scatterings between the barrel and front plate. As the number of bouncing (higher levels) increases, the wave travel path becomes longer so that the scattering point gradually moves toward the far range.

Finally, we simulated the T72 target dataset covering the aspect angles simulated from 0° to 359° with a step of 1° . Figure 16 displays 35 clips for a step of 10° of the aspect angle. With such high-resolution images, the image features are quite different from various angles, which is no surprise since the SAR is sensitive to the target's poses relative to the sensor. From the image set, we can only see the gun structure at angles of 90° and 180° . Some persistent structures of the targets nevertheless show up in the simulated images.

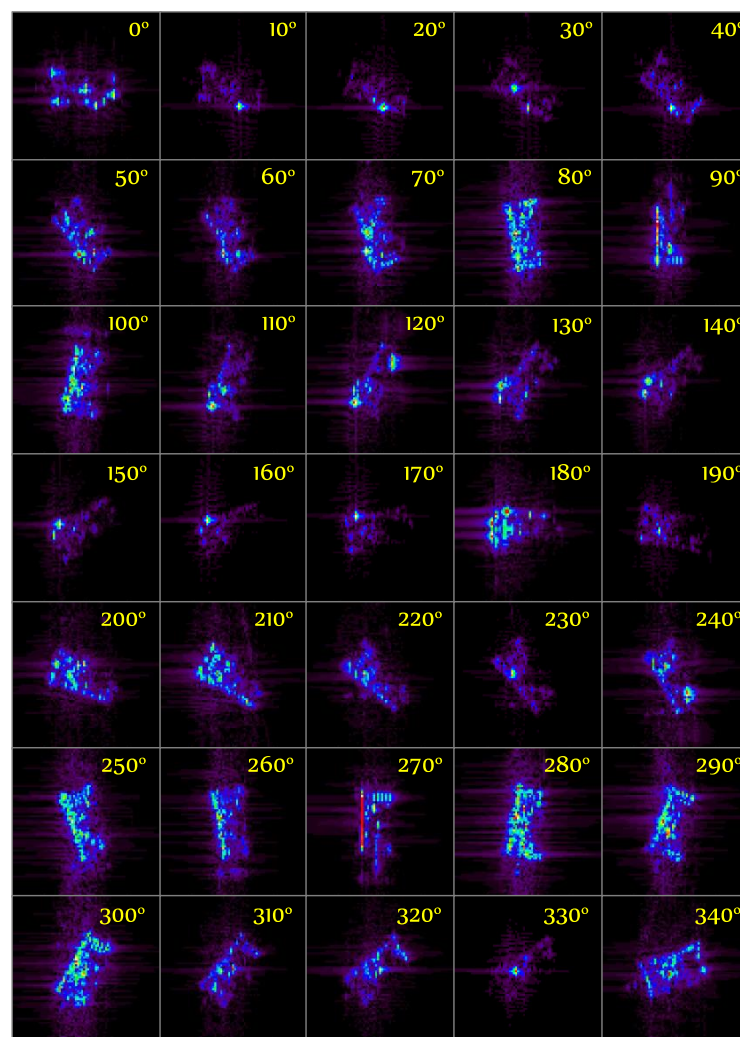


Figure 16. Simulated MSTAR T72 images at various aspect angles from 0° to 340° with a step of 10° .

6. Conclusions

We proposed a GPU-based fast computation of multiple scattering to simulate the SAR image in a coherent system approach. For computing the backscattered fields, we adopted the shooting bouncing ray (SBR), the physical optics (PO), and the physical theory of the diffraction method. To be more realistic, we included the antenna pattern tracking to generate the SAR echo signal. The SAR acquisition mode can be Stripmap or Spotlight. The implementation of the computation parallelization of SAR echo signal generation was demonstrated. By profiling, the overall processing was identified to find which is the heavy loading stage. A dedicated hardware orientation language, NVIDIA CUDA, was adopted. To accommodate the hardware structure, we devised extensive modifications in the CUDA kernel function. We used a GPU card to evaluate the performance of the speedup rate for each modification. Moreover, the accumulated speedup rate was shown in the experiment tables. As a result, the speedup is very high, with over 224 times speedup rate. The computation complexity was demonstrated by comparing the CPU and GPU computations. As a coherent SAR simulator, we included the following chains: SAR returns signal model from targets, whether simple or complex, the range frequency sampling to create the range bin profile, the sensor path trajectory with motion including system error and random noise, the geometry relation between the SAR observation and target, and, finally, image focusing. We then validated the proposed simulation algorithm, using PEC and dielectric spheres, and rotated/unrotated dihedral corner reflectors. We showed that the simulated images by the proposed method have high fidelity in their geometric and radiometric qualities. In particular, the simulator can preserve the polarimetric information of the targets. As an extensive image features database is essential for target detection, identification, and recognition from the SAR image, the fast simulation architecture proposed in this paper fully meets this demand. We will further refine the algorithm to speed up the computation and include other SAR acquisition modes, such as circular SAR and inverse SAR.

Author Contributions: Conceptualization, K.-S.C. and C.-Y.C.; methodology, C.-Y.C. and K.-S.C.; software, C.-Y.C.; validation, C.-Y.C., T.Z. and Y.Z.; formal analysis, C.-Y.C. and K.-S.C.; investigation, C.-Y.C. and Y.Y.; resources, C.-Y.C.; data curation, C.-Y.C.; writing—original draft preparation, K.-S.C. and C.-Y.C.; writing—review and editing, K.-S.C. and Y.Y.; visualization, C.-Y.C., Y.Z. and T.Z.; supervision, K.-S.C.; project administration, K.-S.C.; funding acquisition, K.-S.C. All authors have read and agreed to the published version of the manuscript.

Funding: This work was supported by the initiative funding of Xuchang University to C.Y. Chiang, the Guangxi Natural Science Youth Fund under Grant 2020GXNSFBA297105, and Guangxi Natural Science Fund for Innovation Research Team under Grant 2019GXNSFGA245001.

Institutional Review Board Statement: Not applicable.

Informed Consent Statement: Not applicable.

Data Availability Statement: Not applicable.

Conflicts of Interest: The authors declare no conflict of interest.

References

1. Chen, K.S. *Principles of Synthetic Aperture Radar Imaging: A System Simulation Approach*; CRC Press: Boca Raton, FL, USA, 2016. [[CrossRef](#)]
2. Sheng, Y.; Douglas, E.A. Automated georeferencing and orthorectification of Amazon basin-wide SAR mosaics using SRTM DEM data. *IEEE Trans. Geosci. Remote Sens.* **2005**, *43*, 1929–1940. [[CrossRef](#)]
3. Balz, T. Real-time SAR simulation on graphics processing units. In Proceedings of the 6th European Conference on Synthetic Aperture Radar, Dresden, Germany, 16–18 May 2006.
4. Balz, T.; Uwe, U. Hybrid GPU-based single-and double-bounce SAR simulation. *IEEE Trans. Geosci. Remote Sens.* **2009**, *47*, 3519–3529. [[CrossRef](#)]
5. Mametsa, H.J.; Rouas, F. Imaging radar simulation in realistic environment using shooting and bouncing rays technique. In Proceedings of the SPIE—International Symposium on Remote Sensing, Toulouse, France, 16–21 September 2001; pp. 34–40. [[CrossRef](#)]

6. Hammer, H.; Balz, T. Comparison of SAR simulation concepts for the analysis of high-resolution SAR data. In Proceedings of the 7th European Conference on Synthetic Aperture Radar, Friedrichshafen, Germany, 2–5 June 2008.
7. Holtzman, J.C.; Frost, V.S.; Abbott, J.L.; Kaupp, V.H. Radar image simulation. *IEEE Trans. Geosci. Electron.* **1978**, *16*, 296–303. [[CrossRef](#)]
8. Pike, T.K. A synthetic aperture radar system simulation model: Sarsim. *NASA STI/Recon Tech. Rep. N* **1985**, *86*, 17607.
9. Franceschetti, G.; Migliaccio, M.; Riccio, D.; Schirinzi, G. SARAS: A synthetic aperture radar (SAR) raw signal simulator. *IEEE Trans. Geosci. Remote Sens.* **1992**, *30*, 110–123. [[CrossRef](#)]
10. Margarit, G.; Mallorqui, J.J.; Rius, J.M.; Sanz-Marcos, J. On the usage of GRECOSAR, an orbital polarimetric SAR simulator of complex targets, to vessel classification studies. *IEEE Trans. Geosci. Remote Sens.* **2006**, *44*, 3517–3526. [[CrossRef](#)]
11. Zhu, C.; Xiang, Z.; Wang, K.; Liu, X. A two-level simulator for spaceborne SAR. In Proceedings of the 2009 2nd Asian-Pacific Conference on Synthetic Aperture Radar, Xi'an, China, 26–30 October 2009; pp. 369–372. [[CrossRef](#)]
12. Lu, Y.; Wang, K.; Liu, X.; Yu, W. A GPU based real-time SAR simulation for complex scenes. In Proceedings of the 2009 International Radar Conference Surveillance for a Safer World (RADAR 2009), Bordeaux, France, 12–16 October 2009; pp. 1–4.
13. Zhang, F.; Hu, C.; Li, W.; Hu, W. Accelerating time-domain SAR raw data simulation for large areas using multi-GPUs. *IEEE J. Sel. Top. Appl. Earth Observ. Remote Sens.* **2014**, *7*, 3956–3966. [[CrossRef](#)]
14. Liu, T.; Wang, K.; Liu, X. SAR simulation for large scenes by ray tracing technique based on GPU. In Proceedings of the 2013 IEEE International Geoscience and Remote Sensing Symposium—IGARSS, Melbourne, VIC, Australia, 21–26 July 2013; pp. 1131–1134. [[CrossRef](#)]
15. Yu, L.; Xie, X.; Xiao, L. GPU-accelerated circular SAR echo data simulation of large scenes. In Proceedings of the 2014 31st URSI General Assembly and Scientific Symposium (URSI GASS), Beijing, China, 16–23 August 2014; pp. 1–4. [[CrossRef](#)]
16. Sheng, H.; Zhou, M.; Wang, K.; Liu, X. SAR echo simulation from numerous scattering cells based on GPU. In Proceedings of the IET International Radar Conference 2013, Xi'an, China, 14–16 April 2013; pp. 1–5. [[CrossRef](#)]
17. Sheng, H.; Wang, K.; Liu, X.; Li, J. A fast raw data simulator for the stripmap SAR based on CUDA via GPU. In Proceedings of the 2013 IEEE International Geoscience and Remote Sensing Symposium—IGARSS, Melbourne, VIC, Australia, 21–26 July 2013; pp. 915–918. [[CrossRef](#)]
18. Chen, H.; Huang, Y.; Yang, J. Airborne bistatic SAR echo simulator based on Multi-GPU platform. In Proceedings of the 2011 IEEE CIE International Conference on Radar, Chengdu, China, 24–27 October 2011; pp. 1–5. [[CrossRef](#)]
19. Cumming, I.G.; Wong, F.H.-C. *Digital Processing of Synthetic Aperture Radar Data*; Artech House Publishers: Boston, MA, USA, 2005.
20. Ling, H.; Chou, R.C.; Lee, S.W. Shooting and bouncing rays: Calculating the RCS of an arbitrarily shaped cavity. *IEEE Trans. Antennas Propag.* **1989**, *37*, 194–205. [[CrossRef](#)]
21. Gu, Y.; He, Y.; Fatahalian, K.; Belloch, G. Efficient BVH construction via approximate agglomerative clustering. In Proceedings of the High-Performance Graphics Conference 2013, Anaheim, CA, USA, 19–21 July 2013. [[CrossRef](#)]
22. Zhang, R.; Hong, J.; Ming, F. SAR echo and image simulation of complex targets based on electromagnetic scattering. *J. Electron. Inf. Technol.* **2010**, *32*, 2836–2841. [[CrossRef](#)]
23. Chatzigeorgiadis, F. Development of Code for a Physical Optics Radar Cross Section Prediction and Analysis Application. Ph.D. Thesis, Naval Postgraduate School, Monterey, CA, USA, 2004.
24. Balanis, C.A. *Advanced Engineering Electromagnetics*; Wiley: New York, NY, USA, 2012.
25. De Adana, F.S.; Diego, I.G.; Blanco, O.G. Method based on physical optics for the computation of the radar cross section including diffraction and double effects of metallic and absorbing bodies modeled with parametric surfaces. *IEEE Trans. Antennas Propag.* **2004**, *52*, 3295–3303. [[CrossRef](#)]
26. Knott, E.F.; Senior, T.B.A. Comparison of three high-frequency diffraction techniques. *Proc. IEEE* **1974**, *62*, 1468–1474. [[CrossRef](#)]
27. Knott, E.F.; Schaeffer, J.F.; Tuley, M.T. *Radar Cross Section*; SciTech Press: Raleigh, NC, USA, 2004. [[CrossRef](#)]
28. Model Source. Available online: <https://3dwarehouse.sketchup.com/model/46183323c77488a118ce7b69ff7d764b/T-72-DDR-East-Germany-1985> (accessed on 16 May 2019).
29. MSTAR Source. Available online: <https://www.sdms.af.mil/index.php?collection=mstar> (accessed on 16 May 2019).